

# Vibration signal modeling of a planetary gear set for tooth crack detection



Xihui Liang, Ming J. Zuo\*, Mohammad R. Hoseini

Department of Mechanical Engineering, University of Alberta, Edmonton, Alberta T6G 2G8, Canada

## ARTICLE INFO

### Article history:

Received 3 May 2014

Received in revised form 20 October 2014

Accepted 17 November 2014

Available online 26 November 2014

### Keywords:

Signal modeling  
Dynamic simulation  
Transmission path  
Tooth crack  
Sidebands

## ABSTRACT

In a planetary gearbox, there are multiple vibration sources, and the transmission path of vibration signals changes due to the rotation of the carrier. This study aims to model the vibration signals of a planetary gearbox and investigate the vibration properties in the healthy condition and in the cracked tooth condition. A dynamic model is developed to simulate the vibration source signals. A modified Hamming function is proposed to represent the effect of the transmission path. By incorporating the effect of multiple vibration sources and the effect of transmission path, resultant vibration signals of a planetary gearbox are obtained. Through analyzing the resultant vibration signals, some vibration properties of a planetary gearbox are revealed and the fault symptoms of sun gear tooth crack are identified and located. Finally, the proposed approach is experimentally verified.

© 2014 Elsevier Ltd. All rights reserved.

## 1. Introduction

The vibration signals of a planetary gearbox are more complicated comparing with that of a fixed-shaft gearbox. For a planetary gear set, several sun-planet gear pairs and several ring-planet gear pairs mesh simultaneously. The vibration signals generated by each sun-planet gear pair are similar but with different phases [1]. Similar comments apply to the ring-planet meshes. Due to the phase differences, some of the excitations are canceled or neutralized [2] while others are augmented. In general, vibration transducers, mounted on the housing of a gearbox or the housing of a bearing, are used to acquire vibration signals. Transmission paths of the vibration signals to a transducer change due to the revolution of the carrier. Multiple vibration sources and the effect of the transmission path will cause fault symptoms hard to be distinguished.

Even though many signal processing methods have been proposed to detect gear faults [1–4], the improvements of these methods are still desired. The transducer signal is comprised of many sub signals, such as the vibrations of the sun gear, planet gear, ring gear, bearings and shafts. Unfortunately, there are no mature signal processing methods which can effectively denoise and separate these signals [5,6]. If we can “open” the black box, “see” all the sub-signals, and understand the generation mechanisms of vibration signals, effective tools can be developed to detect gear faults.

Mathematical models have been used by several researchers to investigate the vibration properties of a planetary gearbox [7,8]. However, the mathematical models lack the connection with the physical parameters of a gearbox, like the mesh stiffness and damping. In addition, they can hardly model the process of the fault growth. Dynamic simulation is a better choice to investigate the vibration properties of a planetary gearbox. A dynamic model is more closely connected with the physical

\* Corresponding author. Tel.: +1 780 492 4466; fax: +1 780 492 2200.

E-mail address: [ming.zuo@ualberta.ca](mailto:ming.zuo@ualberta.ca) (M.J. Zuo).

parameters of a planetary gearbox than the mathematical model. It can model the process of fault growth and the corresponding effects. Compared with experimental or field systems, dynamic simulation models have the following advantages [9]: (1) environmental noises can be eliminated so that the changes in vibration signals caused by the faults can be identified easily; and (2) with a good dynamic simulation model, we can easily simulate different types and different levels of faults, and observe changes in the vibration signal due to the faults.

A large range of dynamic models have been developed to simulate the behavior of planetary gears. Kahraman [10] proposed a nonlinear dynamic model to investigate the load sharing characteristics of a planetary gear set. Inalpolat and Kahraman [11] used the same model as Ref. [10] to predict modulation sidebands of a planetary gear set having manufacturing errors. Lin and Parker [12] modified the model of Ref. [10] and investigated the free vibration properties of a planetary gear set. Cheng et al. [13] developed a pure torsional dynamic model to investigate the properties of a planetary gear set when a single pit was present on one tooth of the sun gear. Chaari et al. [14] used a similar model as Ref. [12] to investigate the effect of manufacturing errors on the dynamic behavior of planetary gears. The effects of tooth profile modification or manufacturing errors are not considered in this paper. Studies on the effect of manufacturing error are given in Refs. [11,14] while studies on the effect of tooth profile modification are given in Refs. [15–18].

However, the investigation of the vibration properties of a planetary gearbox with cracked teeth is limited. Barszcz and Randall [19] applied spectra kurtosis to detect a ring gear tooth crack in the planetary gear of a wind turbine. Lewicki et al. [20] utilized vibration separation techniques to detect the tooth damage in the sun gear, planet gear and ring gear, respectively. Chen and Shao [21] investigated the vibration properties of a planetary gear set when there was a tooth root crack in the ring gear. Chaari et al. [22] applied the dynamic model developed in Ref. [14] to investigate the vibration properties of the sun gear and the carrier of a planetary gear set with tooth crack or a single pit on the sun gear. In their studies, the gear mesh stiffness was approximated as a square waveform which would generate unwanted frequency components in the dynamic response [23]. Chen and Shao [24] studied the dynamic features of a planetary gear set when a tooth crack was under different sizes and inclination angles. The displacement signals of the sun gear and the planet gear were investigated when a crack was present on the sun gear or the planet gear. But, Refs. [21,22,24] did not consider the effect of transmission path in their studies. In this study, we focus on cracks in the sun gear only considering the effect of transmission path.

All the above mentioned dynamic models can be divided into two categories: fixed coordinate model and rotating coordinate model. In order to consider inertia effect caused by the rotation of the carrier, a rotating coordinate model is more convenient to use. The inertia force contains gyroscopic force and centrifugal force. Some previous studies [14,24] considered the gyroscopic force in their dynamic models; however, they did not consider the centrifugal force properly in the equilibrium equations of planet gears. In this study, both the gyroscopic force and the centrifugal force will be considered.

A few studies considered the effect of the transmission path in the vibration signal modeling. Inalpolat and Kahraman [7] expressed the resultant acceleration signal of a planetary gear set as follows:

$$a(t) = \sum_{n=1}^N C w_n(t) F_{rpn}(t) \quad (1.1)$$

where  $C$  is a constant;  $N$  represents the number of planet gears;  $w_n(t)$  denotes the effect of transmission path for the  $n$ -th planet gear which is a weighting Hanning function [7] with a time duration of  $T_c/N$ ; and  $F_{rpn}(t)$  is the dynamic force of the  $n$ -th ring-planet mesh.

Later, Inalpolat and Kahraman [11] improved the modeling considering the dynamic forces of both sun-planet meshes and ring-planet meshes. They used the same Hanning function as Ref. [7] to cover the effect of the transmission path.

$$a(t) = \sum_{n=1}^N (C_s w_n(t) F_{spn}(t) + C_r w_n(t) F_{rpn}(t)) \quad (1.2)$$

where  $C_s$  and  $C_r$  are constants facilitated to establish the relation between the gear mesh forces; and  $F_{spn}(t)$  and  $F_{rpn}(t)$  represent the dynamic forces of the  $n$ -th sun-planet mesh and the  $n$ -th ring-planet mesh, respectively.

However, the correctness of Eq. (1.2) is worth discussing. The line of force  $F_{spn}(t)$  is the internal common tangent of the base circles of the sun gear and the  $n$ -th planet gear. While the line of force  $F_{rpn}(t)$  is the internal common tangent of the base circles of the ring gear and the  $n$ -th planet gear. Since dynamic forces  $F_{spn}(t)$  and  $F_{rpn}(t)$  are not in the same direction, it is not proper to add weighted  $F_{spn}(t)$  and weighted  $F_{rpn}(t)$  together as two scalars.

Feng and Zuo [8] investigated possible transmission paths of vibration signals in a planetary gearbox. In Fig. 1, three transmission paths are illustrated from its origin to the transducer. According to their studies, the transducer perceived signal arriving along paths 2 and 3 will have negligible amplitude. Therefore, only the first transmission path was considered in their studies, and the transmission path was modeled by a Hanning function with a time duration of  $T_c$ .

All the previous studies modeled the effect of transmission path using a Hanning function [7,8,11]. They all assumed that as planet  $n$  approached the transducer location, its influence would increase, reaching its maximum when planet  $n$  was the closest to the transducer location, then, its influence would decrease to zero as the planet went away from the transducer. However, even if the planet  $n$  is in the farthest location from the transducer, its influence may not be zero. In this study, we propose an approach to overcome this shortcoming.

In this paper, a planetary gear dynamic model is developed to simulate the vibration signals of each gear, including the sun gear, the planet gears, and the ring gear. In this dynamic model, both the gyroscopic force and the centrifugal force are

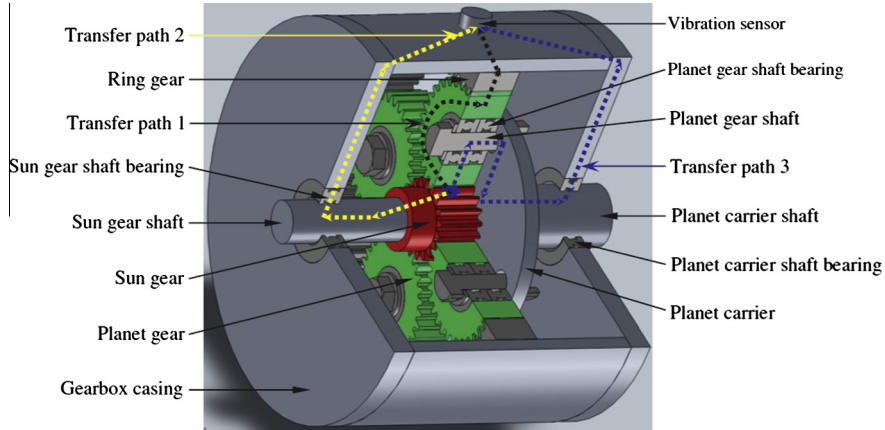


Fig. 1. Transmission paths [8].

considered, and more accurate physical parameters are adopted. The vibration signals are simulated in the perfect condition of a planetary gearbox and in the faulty condition when there is a cracked tooth in the sun gear. A mathematical model is proposed to represent the effect of the transmission path which can fit different planetary gearboxes by choosing proper model parameters. Incorporating the effect of the transmission path, the resultant signals of a planetary gearbox at the transducer location are generated. The vibration signals are investigated both in the time domain and in the frequency domain, and fault symptoms are revealed which can be used to detect the severity of tooth crack. Finally, experimental verification of the proposed approach is performed. Preliminary results of the proposed approach were earlier documented in the technical report [25], and a shorter version of this journal paper is included in the conference proceedings of PHM 2014 [26].

## 2. Dynamic simulation

In this section, a lumped-parameter model is developed to simulate the vibration signals of each gear of a planetary gear set. This model is similar to that used by Lin and Parker [12] with three distinctions: (1) the planet deflections are described in the horizontal and vertical coordinates, (2) both the gyroscopic force and the centrifugal force (inertial force) are incorporated, and (3) more accurate physical parameters are adopted. Whether gear deflections are described in horizontal and vertical coordinates, or radial and tangential coordinates, the gear dynamic behaviors will not be affected. However, the inertial forces may change the dynamic behavior of a gearbox in high speed applications from that at low speeds. Time-varying mesh stiffness is one of the main sources of vibration in a gear transmission system [27]. In Ref. [12], the gear mesh stiffness was approximated by a square waveform. The square waveform reflects only the effect of the change in the tooth contact number, but ignores the effect of the change in the tooth contact position [28]. In addition, the physical damping was ignored in their model. In this study, more accurate physical parameters (mesh stiffness and physical damping) will be adopted in the simulation of vibration signals.

### 2.1. Modeling of a planetary gear set

Fig. 1 shows a two-dimensional lumped-parameter model which is used in this study to simulate the vibration signals of a planetary gear set, which consists of one sun gear ( $s$ ), one ring gear ( $r$ ), one carrier ( $c$ ) and  $N$  planet gears ( $p$ ). Each component has three degrees of freedom: transverse motions in the  $x$ -axis and  $y$ -axis, and rotation. The rotation coordinates  $\theta_i$ ,  $i = s, r, c, p_1, \dots, p_N$  are the angular displacement. The sun gear, ring gear and carrier translations  $x_j, y_j$ ,  $j = s, r, c$  and planet translations  $x_{pn}, y_{pn}$ ,  $n = 1, \dots, N$ , are measured with respect to a rotating frame of reference fixed to the carrier with the origin  $o$ . The gear mesh interface is modeled as a spring-damper system. The directions of all the coordinates at the initial time (time zero) are shown in Fig. 2. Since we are focusing on the effects of a growing crack on the vibration response of the meshing gears, we have ignored the effects of transmission errors in the gears, the frictions between the gear teeth, and other practical phenomena such as backlash. The equations of motion of a planetary gear set are expressed as follows:

Equations of motion for the sun gear:

$$\begin{aligned} m_s \ddot{x}_s + c_{sx} \dot{x}_s + k_{sx} x_s + \sum F_{spn} \cos \psi_{sn} &= m_s \ddot{x}_s \Omega^2 + 2m_s \dot{y}_s \Omega + m_s y_s \dot{\Omega} \\ m_s \ddot{y}_s + c_{sy} \dot{y}_s + k_{sy} y_s + \sum F_{spn} \sin \psi_{sn} &= m_s \ddot{y}_s \Omega^2 - 2m_s \dot{x}_s \Omega - m_s x_s \dot{\Omega} \\ (J_s/r_s) \ddot{\theta}_s + \sum F_{spn} &= T_i/r_s \end{aligned} \quad (2.1)$$

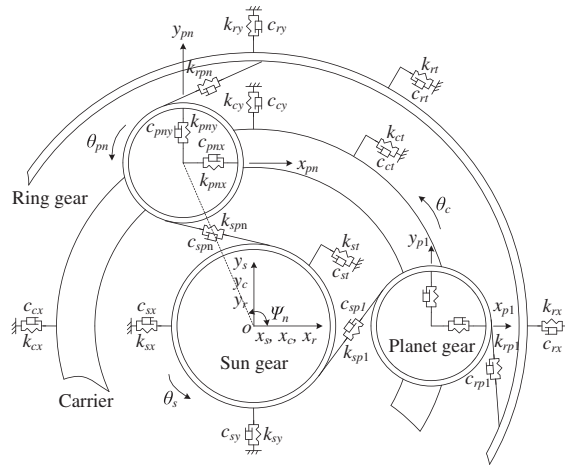


Fig. 2. Dynamic model of a planetary gear set [26].

where  $F_{spn}$  represents the dynamic force of the  $n$ -th sun-planet gear mesh:

$$F_{spn} = k_{spn}\delta_{spn} + c_{spn}\dot{\delta}_{spn}$$

$$\delta_{spn} = (x_s - x_{pn}) \cos \psi_{sn} + (y_s - y_{pn}) \sin \psi_{sn} + r_s \theta_s + r_{pn} \theta_{pn} - r_c \theta_c \cos a$$

$$\psi_{sn} = \pi/2 - a + \psi_n$$

$$\psi_n = 2(n-1)\pi/n; \quad i = 1, 2, \dots, N$$

Equations of motion for the ring gear:

$$m_r \ddot{x}_r + c_{rx} \dot{x}_r + k_{rx} x_r + \sum F_{rpn} \cos \psi_{rn} = m_r x_r \Omega^2 + 2m_r \dot{y}_r \Omega + m_r y_r \dot{\Omega}$$

$$m_r \ddot{y}_r + c_{ry} \dot{y}_r + k_{ry} y_r + \sum F_{rpn} \sin \psi_{rn} = m_r y_r \Omega^2 - 2m_r \dot{x}_r \Omega - m_r x_r \dot{\Omega}$$

$$(J_r/r_r) \ddot{\theta}_r + (c_{rt}/r_r) \dot{\theta}_r + (k_{rt}/r_r) \theta_r + \sum F_{rpn} = 0 \quad (2.2)$$

where  $F_{spn}$  represents the dynamic force of the  $n$ -th sun-planet gear mesh:

$$F_{rpn} = k_{rpn}\delta_{rpn} + c_{rpn}\dot{\delta}_{rpn}$$

$$\delta_{rpn} = (x_r - x_{pn}) \cos \psi_{rn} + (y_r - y_{pn}) \sin \psi_{rn} + r_r \theta_r - r_{pn} \theta_{pn} - r_c \theta_c \cos a$$

$$\psi_{rn} = \pi/2 + a + \psi_n$$

Equations of motion for the planet gears:

$$m_{pn} \ddot{x}_{pn} + F_{cpnx} - F_{spn} \cos \psi_{sn} - F_{rpn} \cos \psi_{rn} = m_{pn} x_{pn} \Omega^2 + 2m_{pn} \dot{y}_{pn} \Omega + m_{pn} y_{pn} \dot{\Omega} + m_{pn} r_c \Omega^2 \cos \psi_n$$

$$m_{pn} \ddot{y}_{pn} + F_{cpny} - F_{spn} \sin \psi_{sn} - F_{rpn} \sin \psi_{rn} = m_{pn} y_{pn} \Omega^2 - 2m_{pn} \dot{x}_{pn} \Omega - m_{pn} x_{pn} \dot{\Omega} + m_{pn} r_c \Omega^2 \sin \psi_n$$

$$(J_{pn}/r_p) \ddot{\theta}_{pn} + F_{spn} - F_{rpn} = 0 \quad (2.3)$$

where  $F_{cpnx}$  and  $F_{cpny}$  describe the bearing forces between the carrier and the  $n$ -th planet in the  $x$  and  $y$  directions:

$$F_{cpnx} = k_{pnx}(x_{pn} - x_c) + c_{pnx}(\dot{x}_{pn} - \dot{x}_c)$$

$$F_{cpny} = k_{pny}(y_{pn} - y_c) + c_{pny}(\dot{y}_{pn} - \dot{y}_c)$$

Equations of motion for the carrier:

$$m_c \ddot{x}_c + c_{cx} \dot{x}_c + k_{cx} x_c - \sum F_{cpnx} = m_c x_c \Omega^2 + 2m_c \dot{y}_c \Omega + m_c y_c \dot{\Omega}$$

$$m_c \ddot{y}_c + c_{cy} \dot{y}_c + k_{cy} y_c - \sum F_{cpsy} = m_c y_c \Omega^2 - 2m_c \dot{x}_c \Omega - m_c x_c \dot{\Omega}$$

$$(J_c/r_c) \ddot{\theta}_c + \sum F_{cpnx} \sin \psi_n - \sum F_{cpny} \cos \psi_n = T_o/r_c \quad (2.4)$$

As a planet gear rotates around the center of the sun gear, the inertial force will be generated. The inertial force contains two items  $m_{pn} x_{pn} \Omega^2$  (gyroscopic force) and  $m_{pn} r_c \Omega^2$  (centrifugal force) which can be observed from the equations of transverse motions of planet gears in Eq. (2.3).  $x_{pn}$ , which is the  $x$ -direction displacement of the  $n$ -th planet gear, is much smaller than  $r_c$  which is the distance between centers of sun gear and planet gear. If  $\cos \psi_n$  takes a value near 1, the item  $m_{pn} r_c \Omega^2 \cos \psi_n$  will dominate the inertial force when the rotation speed of the carrier is large. On the other hand, if  $\cos \psi_n$  takes a small value near 0, the item  $m_{pn} r_c \Omega^2 \sin \psi_n$  will dominate the inertial force when the rotation speed of the carrier is large, but it is in the  $y$ -direction motion. Some previous studies [14,24] considered the gyroscopic force, but ignored the gyroscopic force. In this study, both these two items are considered.

A list of symbols used in this paper is provided at the end of this paper.

## 2.2. Crack modeling and mesh stiffness evaluation

Gear tooth crack is one common failure mode in a gear transmission system. It may occur due to excessive service load, inappropriate operating conditions or simply fatigue [29]. In the dynamic model described in Section 2.1, the gear mesh interface is modeled as a spring-damper system. When a pair of spur gear meshes, the tooth contact number and the tooth mesh position change during meshing. It leads to a periodic variation in the gear mesh stiffness. When a crack happens in one gear tooth, the mesh stiffness will decrease and consequently the vibration properties of the gear system will change. In order to comprehensively understand the vibration properties of a planetary gear set, it is essential to evaluate the mesh stiffness effectively.

According to the research by Belsak and Flasker [30], crack mostly initiates at the critical area of a gear tooth (area of the maximum principle stress), and the propagation paths are smooth, continuous, and in most cases, rather straight with only a slight curvature as shown in Fig. 3. Liang et al. [28] simplified the crack growth path as a straight line starting from the critical area of the tooth root. The same model as Ref. [28] will be used in this study.

The method reported in Ref. [28] will be used directly to evaluate the mesh stiffness of a planetary gear set in the perfect and the cracked tooth condition. Potential energy method [28,31,32] will be applied to evaluate the mesh stiffness of a pair of sun-planet gear and a pair of ring-planet gear. The total potential energy of a pair of meshing gears is considered to be the summation of the Hertzian energy, bending energy, shear energy, and axial compressive energy. The total effective mesh stiffness can be calculated based on the Hertzian, bending, shear, and axial compressive mesh stiffness values. If there is a tooth crack, the bending stiffness and the shear stiffness will reduce due to the change in the tooth length and the tooth height caused by the crack [28], which leads to the decrease of the total mesh stiffness. While each of the sun-planet meshes (or ring-planet meshes) has the same shape of mesh stiffness variation, they are not in phase with each other [33]. Incorporating the mesh phasing relationships, the mesh stiffness of all sun-planet gear pairs and all ring-planet gear pairs can be calculated, thus, the mesh stiffness of a planetary gear set is obtained.

In a planetary gearbox, sun gear teeth easily suffer damage because their multiplicity of meshes with the planet gears increases the potential for damage on the sun gear [2]. Fig. 4 shows the mesh stiffness of a pair of sun-planet gears with

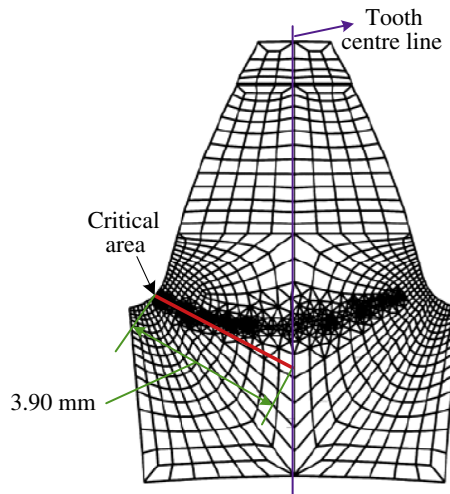


Fig. 3. Tooth crack propagation path [30].

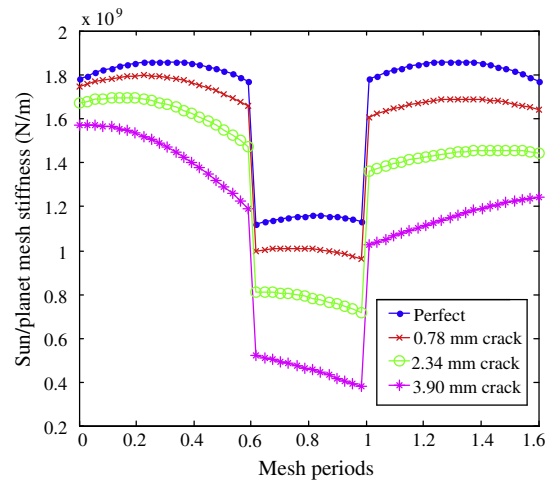


Fig. 4. Mesh stiffness of different crack levels on a sun gear tooth [28].

Table 1  
Physical parameters of a planetary gear set [28].

Parameters	Sun gear	Planet gear	Ring gear
Number of teeth	19	31	81
Module (mm)	3.2	3.2	3.2
Pressure angle	20°	20°	20°
Mass (kg)	0.700	1.822	5.982
Face width (m)	0.0381	0.0381	0.0381
Young's modulus (Pa)	$2.068 \times 10^{11}$	$2.068 \times 10^{11}$	$2.068 \times 10^{11}$
Poisson's ratio	0.3	0.3	0.3
Base circle radius (mm)	28.3	46.2	120.8
Root circle radius (mm)	26.2	45.2	132.6
Reduction ratio	5.263		
Bearing stiffness	$k_{sx} = k_{sy} = k_{rx} = k_{ry} = k_{cx} = k_{cy} = k_{pnx} = k_{pny} = 1.0 \times 10^8 \text{ N/m}$		
Bearing damping	$c_{sx} = c_{sy} = c_{rx} = c_{ry} = c_{cx} = c_{cy} = c_{pnx} = c_{pny} = 1.5 \times 10^3 \text{ Ns/m}$		

different crack levels (perfect, 0.78 mm crack, 2.34 mm crack and 3.90 mm crack) on a sun gear tooth. The physical parameters of this planetary gear set (one sun gear, one fixed ring gear and four equally spaced planet gears) are shown in Table 1. As the growth of the crack, the mesh stiffness reduces gradually, which will cause the gearbox vibrating abnormally.

Fig. 5 describes the mesh stiffness of four sun-planet gear pairs with the consideration of mesh phasing relationships of multiple gear pairs. The curves  $k_{sp1}$ ,  $k_{sp2}$ ,  $k_{sp3}$  and  $k_{sp4}$  represent the 1st, 2nd, 3rd and 4th pair of the sun-planet mesh stiffness, respectively. The mesh stiffness of ring-planet gears are assumed not to be affected by the tooth crack on the sun gear and

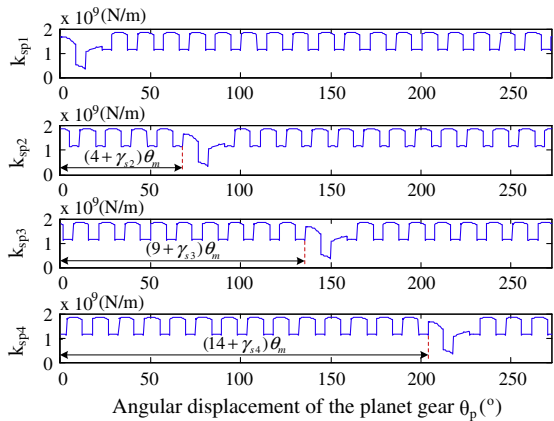


Fig. 5. Mesh stiffness of sun-planet gear pairs with 3.90 mm crack in a sun gear tooth [28].

the stiffness equations of the ring-planet gears were derived in Ref. [28]. The cracked tooth on the sun gear meshes with the four planet gears in turn, therefore, the mesh stiffness of the four pairs of sun-planet gears are all affected. The time intervals of the cracked tooth in meshing are labeled in Fig. 4. The symbol  $\gamma_{sn}$  ( $n = 1, 2, 3, 4$ ) is the relative phase between the  $n$ th sun-planet pair with respect to the 1st sun-planet pair. The value of  $\gamma_{s1}$ ,  $\gamma_{s2}$ ,  $\gamma_{s3}$  and  $\gamma_{s4}$  are 1, 0.75, 0.5 and 0.25, respectively [23]. The symbol  $\theta_m$  denotes the mesh period.

### 2.3. Numerical simulation of vibration signals

In this section, vibration signals of each gear of a planetary gear set are numerically simulated using MATLAB ode15s solver. Physical parameters of the planetary gear set are mainly listed in Table 1. In addition, the mass of the carrier is 10 kg. A constant torque of 450 N m is applied to the sun gear. The rotation speed of the carrier is 8.87 r/min. The gear mesh damping coefficient  $c$  is calculated by the following equation [34]:

$$c = 2\zeta \sqrt{k \frac{m_1 m_2}{m_1 + m_2}} \quad (2.5)$$

where  $k$  denotes the time-varying mesh stiffness of a pair of gear;  $m_1$  and  $m_2$  represent the mass of the pinion and the gear of a pair of gears, respectively;  $\zeta$  is a constant damping ratio which is set to be 0.07 in this study. Through this simulation, the displacement, velocity, and acceleration signals of the sun gear, planet gears, ring gear and carrier are all obtained.

Fig. 6 shows displacement signals of the sun gear in three health conditions: perfect, 0.78 mm crack and 3.90 mm crack in one sun gear tooth. The sun gear has 19 teeth and Fig. 6 illustrates the signals in 19 mesh periods ( $T_m$ ). Within 19 meshes, the cracked tooth will mesh with the four planets in turn. The time duration of the cracked tooth in meshing can be calculated analytically [33]. For the planetary gear set used in this paper, the time duration is 4.75 ( $19/4$ )  $T_m$  which is labeled in Fig. 6. When the cracked tooth is in meshing, the sun gear generates a bigger displacement (fault symptom). With the growth of the crack, the fault symptoms enlarge. However, the fault symptom may appear in the  $x$ -direction displacement or in the  $y$ -direction displacement, even we can see 4 uniformly spaced fault symptoms in the absolute displacement of the sun gear. In the 3.90 mm crack condition, we can observe clearly fault symptoms. However, when the crack length is 0.78 mm, the fault symptom (indicated by the arrows) is very weak. That's why it is hard to detect the fault symptom in the early stage of crack growth.

Fig. 7 depicts the center locus of the sun gear in one revolution of the carrier in three health conditions: perfect, 0.78 mm crack and 3.90 mm crack in one tooth of the sun gear. For this sun gear, the crack length is 3.90 mm when the crack propagates to the tooth center line as indicated in Fig. 3. To demonstrate the fault symptom when there is a small crack, the vibration signals of 0.78 mm (3.90/5 mm) crack are simulated. According to Table 1, the ring gear has 81 teeth, thus in one revolution of the carrier, 81 gear meshes will occur. From Fig. 7, we can see 81 spikes in the perfect condition which correspond to the 81 gear meshes. When there is a crack, some even bigger spikes (fault symptom) can be observed from Fig. 7. In 81 gear meshes, the cracked tooth is involved in meshing in 17 or 18 times ( $81/4.75$ ). 17 bigger spikes are illustrated in the crack condition of Fig. 7. However, when the crack length is 0.78 mm, the fault symptom is weak.

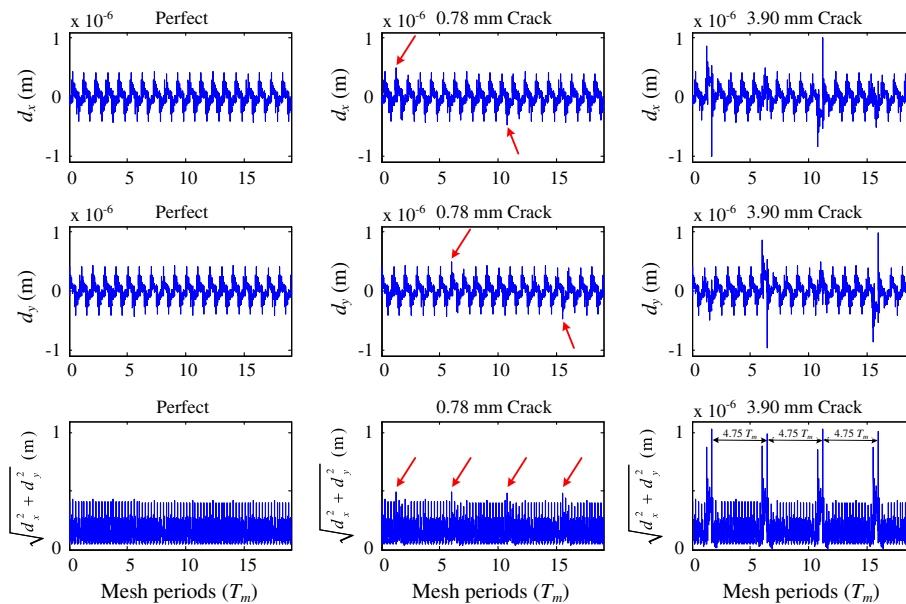


Fig. 6. Displacements of the sun gear at different crack levels  $d_x$ : displacement in the  $x$ -direction;  $d_y$ : displacement in the  $y$ -direction.



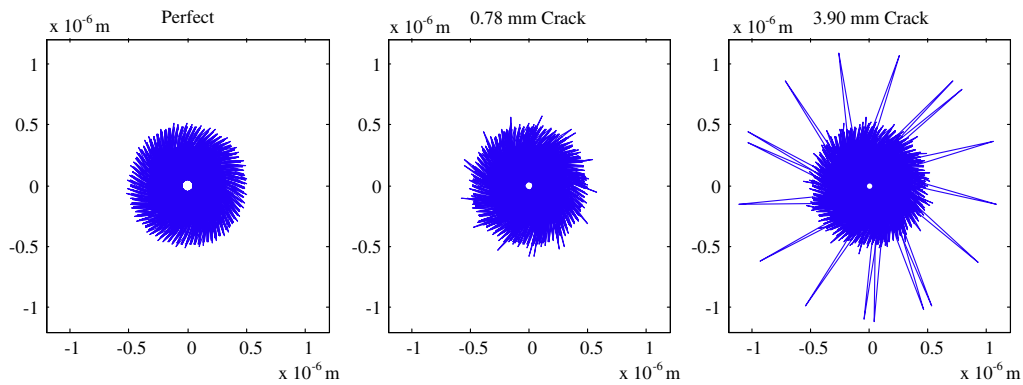


Fig. 7. Center locus of the sun gear.

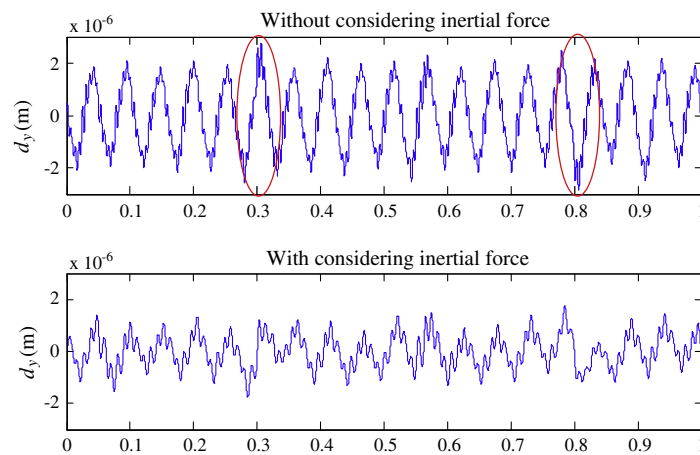


Fig. 8. Y-direction displacement of sun gear with a 2.34 mm crack on a sun gear tooth.

From the displacement signals of the sun gear from Figs. 6 and 7, we can see clear fault symptoms when there is a crack in a sun gear tooth. However, in real applications, it is very hard to acquire the vibration signals of the sun gear. Inside a planetary gearbox, there are multiple vibration sources, because several pairs of sun-planet gears and several pairs of ring-planet gear pairs mesh simultaneously. The vibration signals from these vibration sources will interfere with each other. In addition, due to the rotation of the carrier, the transmission paths of the vibration signals, from the vibration sources to a transducer, change. The effect of the multiple vibration sources and the effect of transmission path will lead to the complexity of the resultant vibration signals acquired by a transducer.

To demonstrate the effects of inertial force (includes the gyroscopic force and the centrifugal force), we compared the dynamic responses of a planetary gearbox in two cases: with considering inertia force and without considering inertia force. When the carrier was running at 8.87 r/min (correspondingly, the sun gear was running at 46.68 r/min), the influence of the inertial force was negligible. The inertial force is not negligible when the rotation speed is large. Fig. 8 shows the Y-direction displacement of the sun gear when the carrier is running at 950 r/min (correspondingly, the sun gear is running at 5000 r/min). There is a 2.34 mm crack in a sun gear tooth. The time duration of the X-axis is one revolution of the sun gear (19 gear meshes).

When the rotation speed of a gearbox is low, the inertial force is small and consequently its influence is very limited. However, with the speed increase of a gearbox, the influence of the inertial force becomes important [12]. As shown in Fig. 8, in the high speed, if the inertial force is incorporated in the dynamic model, the amplitude of gear vibration signal becomes small and the signal oscillation becomes slow. In addition, the fault symptom becomes weak when the inertial force is considered. Thus, it is essential to incorporate the inertial force especially in the high speed applications in order to precisely reflect the real application, because in the real application, the inertial force exists and it never disappears.

### 3. Modeling effect of transmission path

In this study, the resultant vibration signal is considered to be the summation of weighted vibration of each planet gear as shown in Eq. (3.1). The planet gear meshes with the sun gear and the ring gear simultaneously. Therefore, the vibration of the planet gear contains both the information of sun-planet mesh and ring-planet mesh. The effect of the transmission path is



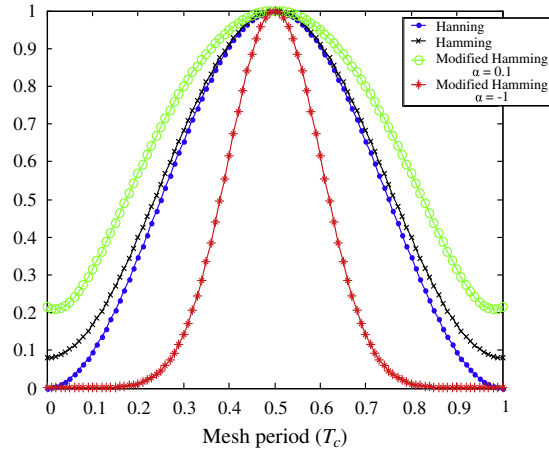


Fig. 9. Modeling effect of transmission paths.

modeled as a modified Hamming function. The exponent expression in Eq. (3.1) can be used to increase or decrease the bandwidth of the Hamming function by choosing different  $\alpha$  values. The value of  $\alpha$  is determined by the properties of a gearbox, like its size, bearing characteristics, ring gear-housing interface and ring gear flexibility. A proper accounting of these effects would require a deformable-body dynamic model that can represent the transfer path between a given gear mesh and the point of measurement accurately [7]. Fig. 9 illustrates the differences of Hanning function, Hamming function and modified Hamming function corresponding to different  $\alpha$  values. The bandwidth is increased when  $\alpha$  is positive, and decreased when  $\alpha$  is negative. However, we need to see that  $\alpha$  cannot take a very large positive value. If  $\alpha$  is very large, the effect of vibration from the farthest planet (distance to the transducer) is amplified, even overweight the effect of vibration from the nearest planet.

$$a(t) = \sum_{n=1}^N e^{\alpha(\text{mod}(w_c t + \psi_n, 2\pi) - \pi)^2} H_n(t) a_n(t) \quad (3.1)$$

where  $H_n(t)$  represents Hamming function for the  $n$ -th planet gear and  $a_n(t)$  is the acceleration signal of the  $n$ -th planet gear.

#### 4. Properties of resultant vibration signals

In this section, resultant vibration signals of a planetary gearbox are obtained and the vibration properties are investigated. Solving the dynamic equations in Section 2.1, we can get acceleration signals of each planet gear in the rotating carrier coordinate system. Applying the theory of acceleration in the rotating coordinate system [35], the absolute acceleration of each planet gear in the coordinate system fixed on the housing of a gearbox can be attained. In this study, only the vertical direction ( $y$ -direction) of the resultant acceleration signals is considered. The resultant acceleration signals of a planetary gearbox in the  $y$ -direction are expressed as the weighted summation of the  $y$ -direction acceleration signal of each planet gear.

Fig. 10 shows the  $y$ -direction acceleration signals of a planetary gearbox at four different cases (the effect of transmission path is represented by a modified Hamming function with  $\alpha = 0.1$ , Hamming function, Hanning function and modified Hamming function with  $\alpha = -1$ ). We can see amplitude modulation in all the cases; however, the degree of the amplitude modulation is different. The amplitude modulation is strongest when the effect of the transmission path is represented by a modified Hamming function with  $\alpha = -1$ . The second strongest one is in the case of Hanning function. The weakest one is in the case of modified Hamming function with  $\alpha = 0.1$ . In addition, we can observe that amplitudes of the vibration signals in the four cases are different. The signal amplitude is largest when the effect of the transmission path is represented by a modified Hamming function with  $\alpha = 0.1$ , while the signal amplitude is smallest when the effect of the transmission path is represented by a modified Hamming function with  $\alpha = -1$ . The advantage of the modified Hamming function is capable of representing the effect of different transmission paths while the Hanning function can represent only one specific transmission path.

However, this study does not intend to propose a method to find the optimum value of  $\alpha$  for a given planetary gearbox. The selection of  $\alpha$  will be investigated in our future work. We have simply tried a few values of  $\alpha$  which are 0.1, 0 and  $-1.0$ . Correspondingly the modified Hamming function has the values of 0.21, 0.08 and 0.03 when the planet gear is in the farthest location from the transducer. The simulated resultant vibration signals for these  $\alpha$  values are presented in Fig. 10. Visually comparing the simulated vibration signals shown in Fig. 10 with the experimental vibration signal in the perfect condition of the gearbox shown in Fig. 16, we believe that the simulated vibration signals match the experimental signals the best when  $\alpha$

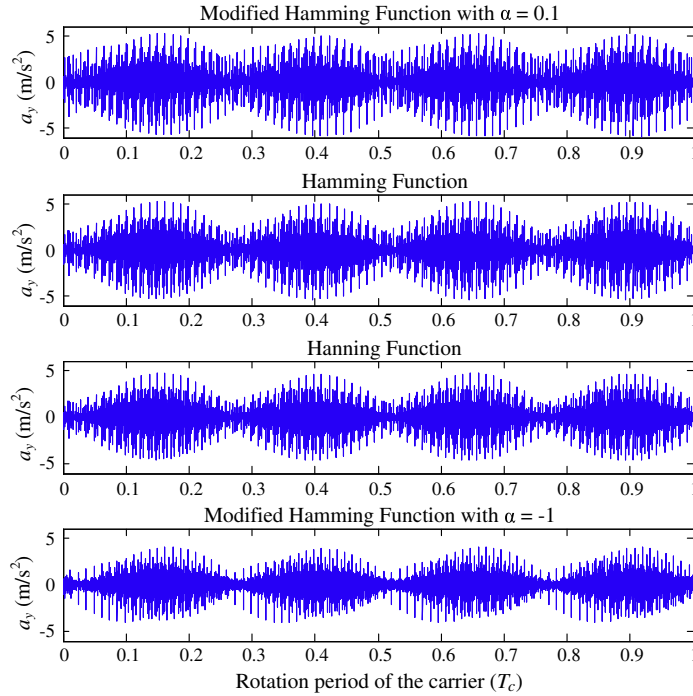


Fig. 10. Simulated resultant vibration signals at different transmission paths.

takes the value of 0.1. Therefore, we have selected  $\alpha$  to be 0.1 in the case study of the revised paper. When  $\alpha$  takes the value of 0.1, it means that 21% of the vibration amplitude of the planet gear which is at the farthest location from the transducer can be sensed by the transducer. In the following discussions, Hamming function ( $\alpha = 0.1$ ) is used to reflect the effect of the transmission path.

Vibration properties of the resultant vibration signals are studied when the planetary gearbox is in three health conditions: perfect, 0.78 mm crack in a sun gear tooth, and 3.90 mm crack in a sun gear tooth. Fig. 11 shows resultant vibration signals of a planetary gearbox (parameters are listed in Table 1). The symbol  $a_y$  represents vertical direction acceleration of the gearbox. Amplitude modulation can be observed both in the perfect condition and in the crack condition. Signal envelope fluctuates four times in one revolution of the carrier as four planets pass through the transducer location sequentially. In the meshing period of the cracked tooth, a bigger spike should be generated. As we know, in one revolution of the carrier, the cracked tooth will mesh 17 or 18 times. When the crack length is 0.78 mm, the fault symptom is very weak. Only three bigger spikes (the locations are indicated by the arrows) can be visually observable. In the 3.90 mm crack condition, 17 bigger spikes are observed. However, some spikes are attenuated strongly (the circled area) due to the effect of the transmission path.

Fig. 12 illustrates the frequency spectrum of the resultant vibration signal in different health conditions. In the perfect condition, there are nearly zero amplitude at the gear mesh frequency  $f_m$  and its harmonics. Sizable amplitudes show in the following locations:  $nf_m$  if  $n$  is an integer and a multiple of 4,  $nf_m \pm f_c$  if  $n$  is an odd integer,  $nf_m \pm 2f_c$  if  $n$  is an even integer but not a multiple of 4. The symbol  $f_c$  denotes rotation frequency of the carrier. In this study, we represent the above mentioned sizable amplitude frequencies by the symbol  $f_{main}$ . This finding confirms the results reported in Ref. [7] that sizable amplitudes appear at carrier order  $H = nN$  in the vicinity of gear mesh frequency and its harmonics ( $n$ : integer,  $N$ : number of planet gears). For example, the largest amplitude frequency  $59f_m + f_c$  locates in the vicinity of 59th harmonic of gear mesh frequency. While,  $59f_m + f_c$  equals to  $4780 f_c$  ( $f_m = 81 f_c$ ) which is the location of 4780 carrier order. The number 4780 is a multiple of 4 which is the number of planet gears. We also can observe from Fig. 12 that if there is crack on a sun gear tooth, the amplitude of frequencies  $f_{main}$  are rarely affected. However, a lot of sidebands appear in the vicinity of  $f_{main}$ .

Fig. 13 presents the zoomed-in plot of the frequency region from  $42f_m$  to  $44f_m$ . We can see a large amount of sidebands appear but they are not symmetric. Sizable sidebands appear in the following locations:  $f_{main} \pm kf_{scrack} \pm mf_s \pm nf_p \pm f_c$  ( $k, m$ , and  $n$  are integers). For the planetary gear set used in this study,  $k, m$ , and  $n$  can take the following values:  $k = 0, 1, 2, 3, 4$ ;  $m = 0, 1, 2$ ;  $n = 0, 1, 2, 3, 4$ .  $f_s$  and  $f_p$  denotes the rotation frequency of the sun gear and the planet gear, respectively, while  $f_{scrack}$  represents the characteristic frequency of the cracked sun gear, which can be calculated as follows [8]:

$$f_{scrack} = f_m \times N/Z_{sun} \quad (4.1)$$

where  $N$  represents the number of planet gears and  $Z_{sun}$  denotes the teeth number of sun gear.

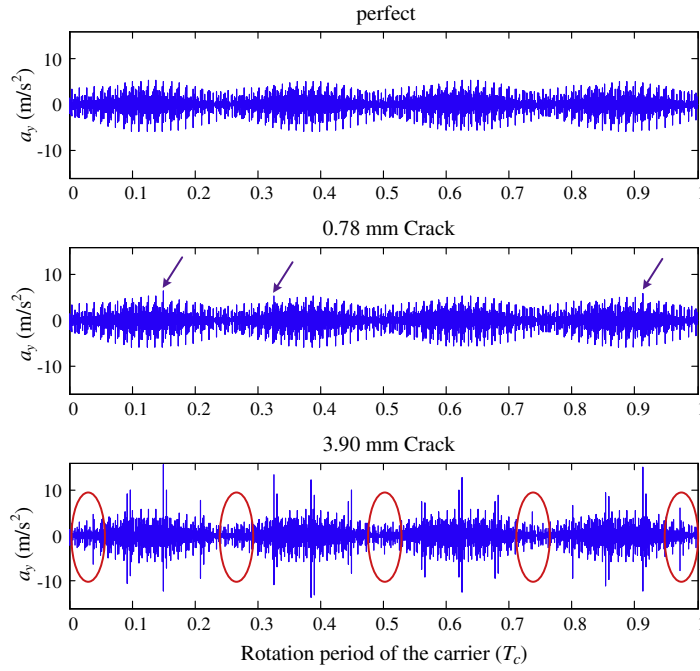


Fig. 11. Simulated resultant vibration signals in the y-direction.

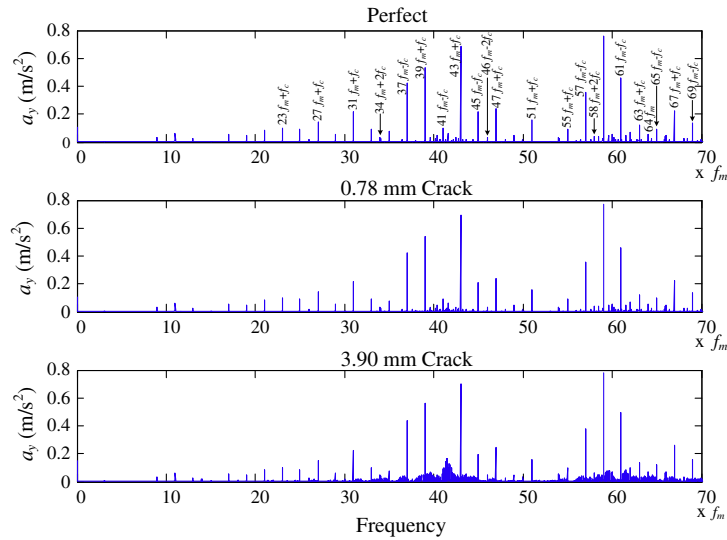


Fig. 12. Frequency spectrum of simulated resultant vibration signals.

## 5. Experimental verification

Experimental signals are acquired from a gearbox test rig to verify the simulated resultant vibration signals and the fault symptoms revealed in this study. The configuration of the test rig is shown in Fig. 14 and the parameters of gears are listed in Table 2. All the experimental gears are standard spur gears without tooth profile modification. In addition, we assume that all gears are perfect without manufacturing errors. An acceleration sensor is installed in the vertical direction of the casing of the second stage planetary gearbox to acquire the vibration signals. The simulated planetary gear set has the same configuration and gear parameters as the second stage planetary gear set. The vibration data was acquired when the rotation frequency of the motor was 1200 r/min. Thus, the rotation speed of the sun gear of the second stage planetary gearbox is 46.66 r/min which is the same as the simulated sun gear speed in Section 2.3. To simulate the crack effect on the vibration

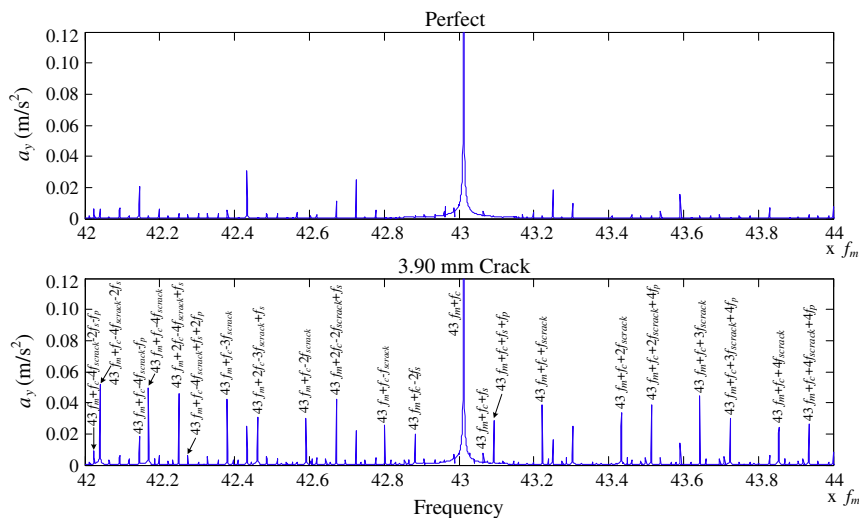


Fig. 13. Zoomed-in frequency spectrum of simulated resultant vibration signals.

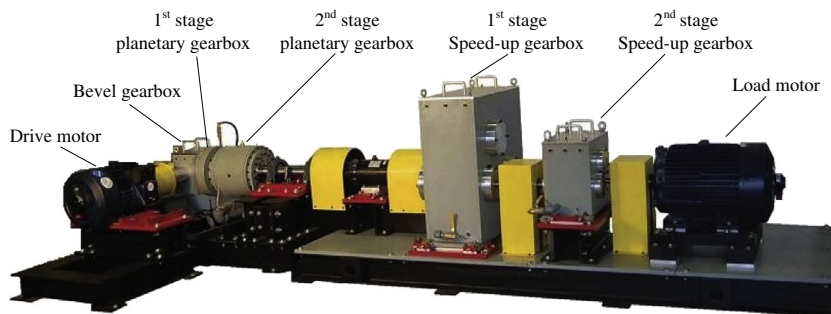


Fig. 14. Experimental test rig.

Table 2

Parameters of experimental test rig.

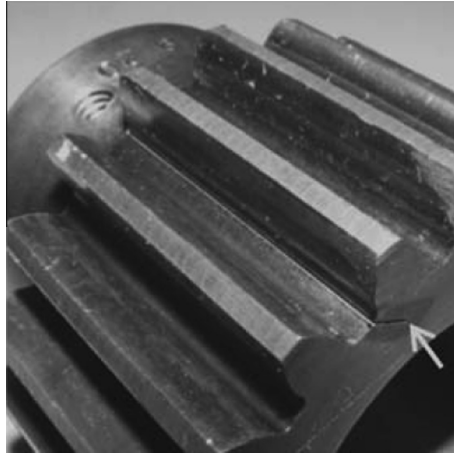
Gearbox	Bevel stage		First stage planetary gearbox			Second stage planetary gearbox		
Gear	Input	Output	Sun	Planet	Ring	Sun	Planet	Ring
No. of teeth	18	72	28	62 (4)	152	19	31 (4)	81

Note: The number of planet gears is indicated in the parenthesis.

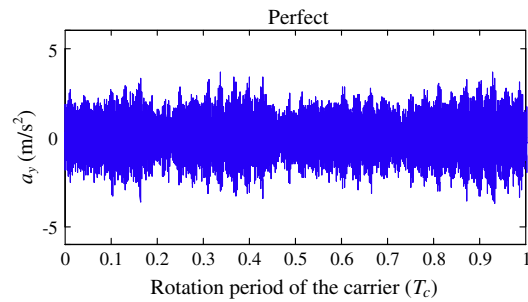
signals, tooth crack was manually created in the sun gear tooth using the electro discharge machining. When the crack length is small, fault symptoms may submerge in the noise and hard to distinguish. To amplify the fault symptoms, 3.9 mm tooth crack was created in the sun gear tooth. The crack goes through the whole tooth width as shown in Fig. 15.

Fig. 16 shows the experimental acceleration signals of the second stage planetary gearbox in the perfect condition. The symbol  $a_y$  denotes the vertical direction acceleration of the gearbox. Amplitude modulation presents in the perfect condition of the gearbox and signal envelope fluctuates four times in one revolution of the carrier. Fig. 17 describes the experimental acceleration signals of the second stage planetary gearbox both in the perfect condition and in the cracked tooth condition. In the cracked tooth condition, some even bigger spikes show up. In addition, the amplitude modulation is not very obvious, as amplitude modulation and fault signatures together lead to the complexity of the vibration signals.

Fig. 18 illustrates the frequency spectrum of the experimental signals. In the perfect condition, sizable amplitudes show in the following locations ( $f_{main}$ ):  $nf_m$  if  $n$  is an integer and a multiple of 4,  $nf_m \pm f_c$  if  $n$  is an odd integer,  $nf_m \pm 2f_c$  if  $n$  is an even integer but not a multiple of 4. When crack is in the sun gear tooth, many sidebands show in the vicinity of  $f_{main}$  which is most obvious in the region of  $40f_m$ – $50f_m$ . Fig. 19 presents the zoomed-in frequency spectrum of the experimental signals from  $42f_m$  to  $44f_m$ . The sidebands are asymmetric and sizable sidebands appear in the following locations:  $f_{main} \pm kf_{crack} \pm$



**Fig. 15.** 3.9 mm manually made tooth crack in the sun gear.



**Fig. 16.** Experimental resultant vibration signals in perfect condition.

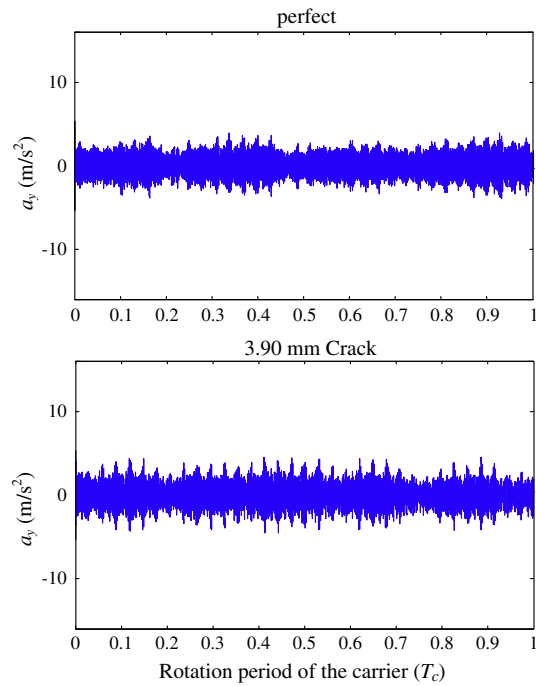


**Fig. 17.** Experimental resultant vibration signals in perfect and crack conditions.

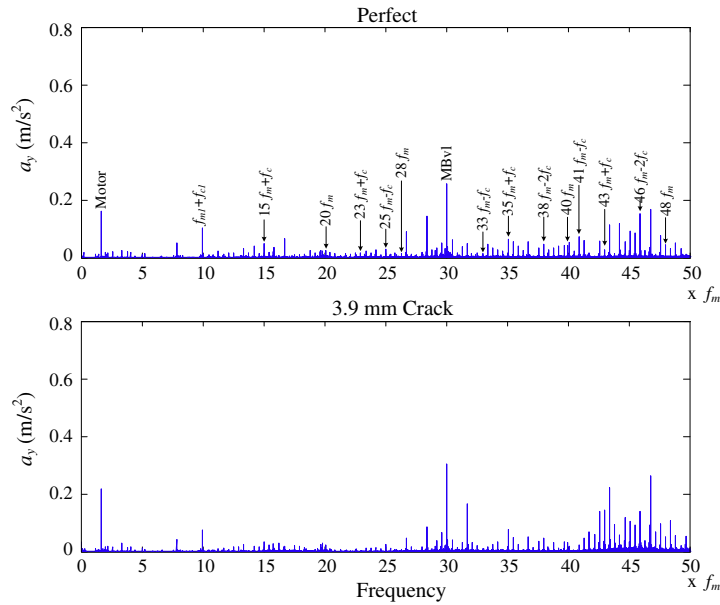


Fig. 18. Frequency spectrum of experimental vibration signals.

$mf_s \pm nf_p \pm f_c$ . The integers of  $k$ ,  $m$ , and  $n$  take the following values:  $k = 0, 1, 2, 3, 4$ ;  $m = 0, 1, 2$ ;  $n = 0, 1, 2, 3, 4$ . These results confirm the proposed result in Section 4.

In this paragraph, the amplitudes of the simulated vibration signals and experimental signals are compared. In the time domain, the maximum amplitude of the simulated signal is about  $5 \text{ m/s}^2$  when the gearbox is perfect as shown in Fig. 11. By contrast, the maximum amplitude of the experimental signal is about  $4 \text{ m/s}^2$  when the gearbox is perfect as shown in Fig. 17. In the condition of 3.90 mm crack, some bigger spikes (fault symptom) are generated in the simulated signal. The amplitude of the bigger spikes reaches to about  $10 \text{ m/s}^2$ . In the experimental signal of 3.90 mm crack, we can see some bigger spikes present. But the amplitude of these spikes is only about  $5 \text{ m/s}^2$ . In the frequency domain of a healthy gearbox, the amplitude of sizable frequency components reaches up to  $0.8 \text{ m/s}^2$ . However, the amplitude of experimental signals reaches to only  $0.2 \text{ m/s}^2$ . When there is 3.90 mm crack in a sun gear tooth, there is no big change of the amplitude of sizable frequency components both in the simulated signals and in the experimental signals. Some sidebands appear both in the simulated signals and experimental signals. The amplitude difference of sidebands of simulated signals and experimental signals is small. The amplitude of most of the sidebands is below  $0.05 \text{ m/s}^2$  both in the simulated signals and experimental signals. Only three sidebands are over  $0.05 \text{ m/s}^2$  in the experimental signals, namely  $43f_m + f_c - 2f_{\text{crack}}$ ,  $43f_m + f_c + 2f_{\text{crack}}$ , and  $43f_m + f_c + 2f_{\text{crack}}$ . There are three possible reasons to explain the amplitude differences between the numerical and experimental results. Firstly, the numerical model only simulated one stage of planetary gearbox. While the experimental test rig is quite complicated. It includes one stage of bevel gear, two stages of planetary gearboxes and two stages of fixed shaft gearboxes. Secondly, the shaft mass is not considered in the simulated model, while in the test rig, a very heavy shaft going through the whole system. The big mass of the shaft will damp the amplitude of the vibration. Thirdly, the dynamic model did not consider the damping effect of the connection between gearbox housing and the ground. The gearbox test rig is fixed

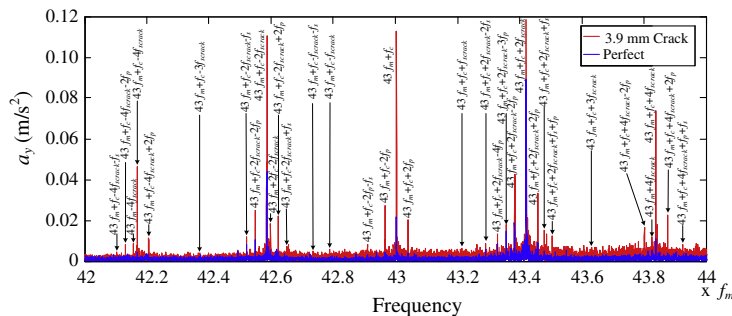


Fig. 19. Zoomed-in frequency spectrum of experimental vibration signals.

on the ground by several screws. The damping effect of the screw will also damp the amplitude of the vibration. All these damping effect will limit the amplitude of big spikes. The proposed model reveals some properties of a stage of planetary gearbox; however, efforts are still needed to improve the numerical model, like reducing the amplitude difference between the numerical signals and experimental signals.

## 6. Conclusion

In this study, a theoretical model is proposed to simulate the resultant vibration signals of a planetary gearbox in the healthy condition and the cracked tooth condition. A lumped-parameter model is developed to simulate the vibration signals of each gear, including the sun gear, planet gears and ring gear. A mathematical model is proposed to consider the effect of the transmission path. Incorporating the effect of multiple vibration sources and the effect of the transmission path, the resultant vibration signals at the sensor location are obtained. In the time domain, obvious fault symptoms show in the vibration signals of an individual gear, like the sun gear. However, the fault symptoms attenuate in the resultant vibration signal. Besides, obvious amplitude modulation is observed in the resultant vibration signal due to the rotation of the carrier. In the frequency domain, a large amount of sidebands appear when there is a crack in the sun gear tooth. These sidebands are investigated and located, which can be used to detect the crack fault. The simulated resultant signals are verified both in the time domain and in the frequency domain by comparing with the experimental signals.

## Acknowledgements

This research is supported by the Natural Science and Engineering Research Council of Canada (NSERC) and China Scholarship Council (CSC). Comments and suggestions from reviewers and the Editor are very much appreciated.

## Appendix A

Notation	
$a$	pressure angle of gear pairs
$c_{sx}, c_{sy}$	damping coefficient of sun gear bearing in the $x, y$ direction
$c_{rx}, c_{ry}$	damping coefficient of ring gear bearing in the $x, y$ direction
$c_{cx}, c_{cy}$	damping coefficient of carrier bearing in the $x, y$ direction
$c_{pnx}, c_{pny}$	damping coefficient of $n$ -th planet in the $x, y$ direction
$c_{spn}, c_{rpn}$	mesh damping coefficient of $n$ -th sun-planet, ring-planet
$c_{rt}$	damping coefficient of ring gear in torsional direction
$f_m$	gear mesh frequency
$f_{main}$	sizable amplitude frequencies when the gearbox is in perfect condition
$f_s, f_p, f_c$	rotational frequency of the sun gear, planet gear, carrier
$f_{scrack}$	characteristic frequency of the cracked sun gear tooth
$J_s, J_p, J_r, J_c$	mass moment of inertia of the sun gear, planet gear, ring gear, carrier
$h_n(t)$	Hanning function: $h_n(t) = 0.5 - 0.5 \cos(\omega_c t + \psi_n)$
$H_n(t)$	Hamming function: $H_n(t) = 0.54 - 0.46 \cos(\omega_c t + \psi_n)$
$m_s, m_p, m_r, m_c$	mass of the sun gear, planet gear, ring gear, carrier
$N$	number of planet gears in a planetary gear set
$k_{sx}, k_{sy}$	stiffness of sun gear bearing in the $x, y$ direction
$k_{rx}, k_{ry}$	stiffness of ring gear bearing in the $x, y$ direction
$k_{cx}, k_{cy}$	stiffness of carrier bearing in the $x, y$ direction
$k_{pnx}, k_{pny}$	stiffness of $n$ -th planet bearing in the $x, y$ direction
$k_{spn}, k_{rpn}$	mesh stiffness of $n$ -th sun-planet, ring-planet
$k_{rt}$	stiffness of ring gear in torsional direction
$r_s, r_p, r_r$	base circle radius of the sun gear, planet gear, ring gear
$r_c$	radius of the circle passing through planet gear centers
$T_c$	rotational period of the carrier
$T_m$	gear mesh period
$T_i, T_o$	input torque on the sun gear, output torque on the carrier
$Z_s, Z_p, Z_r$	the number of tooth of the sun gear, planet gear, ring gear
$\delta_{spn}, \delta_{rpn}$	relative displacement on the lines of action of $n$ -th sun-planet, ring-planet
$\psi_n$	circumferential angle of $n$ -th planet
$\Omega$	rotation speed of the carrier



## References

- [1] Blunt DM, Keller JA. Detection of a fatigue crack in a UH-60A planet gear carrier using vibration analysis. *Mech Syst Signal Process* 2006;20:2095–111.
- [2] Lei Y, Kong D, Lin J, Zuo MJ. Fault detection of planetary gearboxes using new diagnostic parameters. *Meas Sci Technol* 2012;23(5):1–10.
- [3] Liu J, Wang W, Golnaraghi F. An extended wavelet spectrum for bearing fault diagnostics. *IEEE T Instrum Meas* 2008;57(12):2801–12.
- [4] Jardine AKS, Lin D, Banjevic D. A review on machinery diagnostics and prognostics implementing condition-based maintenance. *Mech Syst Signal Process* 2006;20(7):1483–510.
- [5] Antoni J. Blind separation of vibration components: principles and demonstrations. *Mech Syst Signal Process* 2005;19:1166–80.
- [6] Zhang B, Khawaja T, Patrick R, et al. A novel blind deconvolution de-noising scheme in failure prognosis. *Trans Inst Meas Control* 2010;32(1):3–30.
- [7] Inalpolat M, Kahraman A. A theoretical and experimental investigation of modulation sidebands of planetary gear sets. *J Sound Vib* 2009;323:677–96.
- [8] Feng Z, Zuo MJ. Vibration signal models for fault diagnosis of planetary gearboxes. *J Sound Vib* 2012;331:4919–39.
- [9] Tian Z, Zuo MJ, Wu S. Crack propagation assessment for spur gears using model-based analysis and simulation. *J Intell Manuf* 2009;23(2):239–53.
- [10] Kahraman A. Load sharing characteristics of planetary transmissions. *Mech Mach Theory* 1994;29:1151–65.
- [11] Inalpolat M, Kahraman A. A dynamic model to predict modulation sidebands of a planetary gear set having manufacturing errors. *J Sound Vib* 2010;329:371–93.
- [12] Lin J, Parker RG. Analytical characterization of the unique properties of planetary gear free vibration. *J Vib Acoust* 1999;121(3):316–21.
- [13] Cheng Z, Hu N, et al. Pitting damage levels estimation for planetary gear sets base on model simulation and grey relational analysis. *Trans Can Soc Mech Eng* 2011;35(3):403–17.
- [14] Chaari F, Fakhfakh T, Hbaieb R, Louati J, Haddar M. Influence of manufacturing errors on the dynamical behavior of planetary gear. *Int J Adv Manuf Tech* 2006;6(6):738–46.
- [15] Eritenel T, Parker RG. Nonlinear vibration of gears with tooth surface modifications. *J Vib Acoust* 2013;135(5):1–11.
- [16] Bahk CJ, Parker RG. Analytical investigation of tooth profile modification effects on planetary gear dynamics. *Mech Mach Theory* 2013;70:298–319.
- [17] Chen Z, Shao Y. Mesh stiffness calculation of a spur gear pair with tooth profile modification and tooth root crack. *Mech Mach Theory* 2013;62:63–74.
- [18] Chen Z, Shao Y. Dynamic features of planetary gear set with tooth plastic inclination deformation due to tooth root crack. *Nonlinear Dyn* 2013;74(4):1253–66.
- [19] Barszcz T, Randall RB. Application of spectral kurtosis for detection of a tooth crack in the planetary gear of a wind turbine. *Mech Syst Signal Process* 2009;23(4):1352–65.
- [20] Lewicki DG, LaBerge KE, Ehinger RT, Fetty J. Planetary gearbox fault detection using vibration separation techniques. In: 67th Annual forum and technology display, Virginia Beach, Virginia, 3–5 May; 2011.
- [21] Chen Z, Shao Y. Dynamic simulation of planetary gear with tooth root crack in ring gear. *Eng Fail Anal* 2013;31:8–18.
- [22] Chaari F, Fakhfakh T, Haddar M. Dynamic analysis of a planetary gear failure caused by tooth pitting and cracking. *J Fail Anal Prev* 2006;6:73–8.
- [23] Liang X, Zuo MJ, Patel TH. Evaluating the time-varying mesh stiffness of a planetary gear set using the potential energy method. *Proc Inst Mech Eng C-J Mech Sci* 2014;228:535–47.
- [24] Chen Z, Shao Y. Dynamic features of a planetary gear system with tooth crack under different sizes and inclination angles. *J Vib Acoust* 2013;135:1–12.
- [25] Hoseini M, Patel TH, Liu Z, Zhao X, Moghaddass R, Liang X, Zuo MJ. Dynamic simulation of planetary gearsets. Technical Report, Department of Mechanical Engineering, University of Alberta, Edmonton, Alberta; 2011.
- [26] Liang X, Zuo MJ, Hoseini MR. Understanding vibration properties of a planetary gear set for fault detection. In: IEEE international conference on prognostics and health management, Spokane, Washington, USA, 22–25 June; 2014.
- [27] Eritenel T, Parker RG. An investigation of tooth mesh nonlinearity and partial contact loss in gear pairs using a lumped-parameter model. *Mech Mach Theory* 2012;56:28–51.
- [28] Liang X, Zuo MJ, Pandey M. Analytically evaluating the influence of crack on the mesh stiffness of a planetary gear set. *Mech Mach Theory* 2014;76:20–38.
- [29] Chaari F, Baccar W, Abbes MS, Haddar M. Effect of spalling or tooth breakage on gearmesh stiffness and dynamic response of a one-stage spur gear transmission. *Eur J Mech A-Solid* 2008;27:691–705.
- [30] Belsak A, Flaker J. Detecting cracks in the tooth root of gears. *Eng Fail Anal* 2007;14:1466–75.
- [31] Yang DCH, Lin JY. Hertzian damping, tooth friction and bending elasticity in gear impact dynamics. *J Mech Trans-T ASME* 1987;109:189–96.
- [32] Wu S, Zuo MJ, Parey A. Simulation of spur gear dynamics and estimation of fault growth. *J Sound Vib* 2008;317:608–24.
- [33] Parker RG, Lin J. Mesh phasing relationships in planetary and epicyclic gears. *J Mech Des* 2004;126:365–70.
- [34] Inman DJ. Engineering vibration. Prentice Hall; 1994.
- [35] Hibbeler RC. Dynamics. 3rd ed. Pearson Prentice Hall; 2004.